Small-scale flow topologies in decaying isotropic turbulence laden with finite-size droplets

Michael S. Dodd* and Lluís Jofre†
Center for Turbulence Research, Stanford University, Stanford, California 94305, USA

(Received 10 January 2019; published 13 June 2019)

The topology of the fine-scale motions in decaying isotropic turbulence laden with droplets of super-Kolmogorov size is investigated using results from direct numerical simulations. The invariants of the velocity-gradient, rate-of-strain, and rate-of-rotation tensors are computed in the carrier phase. The joint probability density functions of the invariants are calculated and conditioned on different distances from the droplet surface. The results show that outside the viscous region near the interface, the flow topologies favor stable focus/stretching and unstable node/saddle/saddle structures, which is in agreement with those found in canonical homogeneous isotropic turbulence. Inside the viscous layer at the droplet surface, the flow topologies shift from a preference for high-enstrophy/low-dissipation motions to favoring low-enstrophy/high-dissipation. At the droplet surface, there is a strong tendency for boundary-layer-like and vortex-sheet flow topologies in which the strain and rotation rates are positively correlated. An interesting observation is that the shapes of the invariant distributions at the droplet surface are remarkably similar to those reported in the viscous sublayer of turbulent wall-bounded flows. Also, the results show that the smallest hydrodynamic length scale of the carrier fluid turbulence is located at the droplet interface and that this length scale is two to three times smaller than that of the surrounding bulk flow. From a computational viewpoint, this suggests a more stringent spatial resolution requirement for the direct numerical simulation of finite-size droplets in isotropic turbulence than its single-phase counterpart.

DOI: 10.1103/PhysRevFluids.4.064303

I. INTRODUCTION

Droplet-laden turbulent flows are important in numerous industrial and natural processes, such as spray combustion [1] and rain formation [2]. As a result of the consistent rise of computing power over the past decades, the use of computational approaches have become an indispensable tool for the analysis and design of such complex systems. Direct numerical simulation (DNS), resolving all length and timescales of turbulent flows interacting with interfaces without significant modeling assumptions, is now feasible for moderate Reynolds number [3] or for reduced computational complexity (i.e., interfaces undergoing small deformation and/or limited number of droplets/bubbles) two-phase flows [4]. The case investigated in this work is of the former category—complex two-phase flow involving many droplets, but with moderate Reynolds number. While this study is primarily aimed at improving the fundamental understanding of turbulent flow structures in the vicinity of two-phase interfaces (e.g., boundary layers and wakes), the insights are expected to be useful also for reduced-order and subgrid-scale (SGS) modeling. Particular focus is placed on two-phase interface dynamics and associated turbulent kinetic energy (TKE) dissipation

*doddm@stanford.edu
†jofre@stanford.edu

mechanisms. An accurate reproduction of such effects is of central importance with regards to the dynamics and energetics of droplet-laden turbulent flows.

Turbulence modeling in dispersed multiphase flows remains an outstanding challenge, especially when the dispersed phase has characteristic sizes larger than the smallest length scales of the flow, rendering a point particle approximation inaccurate. As a result, the development of predictive, coarse-grained models for design and optimization of engineering applications, such as, Reynolds-averaged Navier-Stokes (RANS) approaches, remains an open problem. It is now well established that, since the large-scale features of turbulence are typically flow dependent, different models are needed for different flows [5]. However, a major motivation for the development of large-eddy simulation (LES) approaches is the belief that, although large structures may vary between flows, at smaller scales the features should be less flow-dependent and more amenable to modeling. This belief in the fine-scale universality of turbulent flows is supported by evidence from investigations in the past decades, e.g., [6–10]. Universal fine-scale features, if they can be identified, should potentially be of greater utility in construction of SGS models than broad assumptions concerning statistical isotropy of turbulent fluctuations at high wave numbers [11,12]. For example, in the case of finite-size droplets and particles, it is unclear whether the small scales are universal and statistically isotropic. In particular, a question arises concerning how the structure of the turbulence changes with respect to distance from the dispersed phase.

Computational studies have shown that the introduction of finite-size particles, or droplets, into isotropic turbulence increases the decay rate of TKE [3,13], and that this increase is primarily due to enhanced dissipation at the particle/droplet surface. In Ref. [13], by conditionally averaging the dissipation rate and the velocity-gradient tensor eigenvalues on distance from the particle surface, it was shown that the particle augments the dissipation rate by increasing both the extensional and compressive eigenvalues near the particle surface. An analogous study in droplet-laden isotropic turbulence has yet to be performed. Droplets introduce additional physical mechanisms into the flow compared to solid particles due to the droplet's ability to deform, breakup, coalesce with other droplets, and develop internal fluid motion.

Local topology, or streamline patterns, is notably useful for characterizing flow features and regimes as it is very efficient in quantifying the levels of fluid element deformation and mixing. For example, a strain-dominated streamline pattern will deform a fluid element and lead to increased mixing, while a rotation-dominated pattern, on the other hand, will merely reorient a fluid element without much increase in mixing. Motivated by the need of a general methodology, Perry, Chong, and Cantwell [14,15] proposed a scheme based on the three invariants (P, Q, R) of second-order tensors to effectively infer local flow topologies in velocity fields. Subsequently, Soria *et al.* [16], using DNS results, studied the joint statistical distributions of Q and R in mixing layers. They found that the scatter plot of second and third invariants (i) presents small amounts of data in the lower right quadrant, whereas (ii) the bulk of data lies in the upper left and lower right quadrants roughly distributed uniformly over an elliptical region. The local topologies associated with these two regions are unstable node/saddle/saddle and stable focus stretching (described in detail later). These prominent topological features immediately attracted considerable research attention and were later found to be quite general across a variety of turbulent flows. Examples of such studies include high-symmetry flows [17], turbulent boundary layers [18], turbulent channel flows [19], turbulent jets [20], and compressible turbulence [21]. For a review of the dynamics of small-scale turbulence and various modeling approaches we refer the reader to the article by Meneveau [22]. In the context of multiphase flows, the methodology has been recently applied, for instance, to analyze the flow structures in turbulence generated by rising bubbles [4,23]. The utility of correctly predicting small-scale flow topologies has been demonstrated in LES of droplet-laden turbulent channel flow, where the microphysics of sub-Kolmogorov size, inertialess droplets was captured in the one-way coupled regime using a subgrid-scale model for the evolution of the velocity-gradient tensor [24]. However, to the best of the authors' knowledge, this paper is the first work to characterize the flow structures in the vicinity of finite-size droplets in homogeneous isotropic turbulence (HIT).

This paper is organized as follows. Section II provides an overview of the methodology utilized to infer the local flow topology based on velocity-gradient invariants. Next, in Sec. III, a description of the droplet-laden HIT dataset considered in this work is given. Results and important findings are discussed in Sec. IV. Finally, conclusions are drawn and future work is proposed in Sec. V.

II. CLASSIFICATION OF LOCAL FLOW TOPOLOGY

The use of DNS to study the velocity-gradient statistics in turbulent flows has been primarily confined to single-phase flows. The theoretical work that connected invariants of the velocity-gradient tensor to flow topologies was established by Perry, Chong, and Cantwell [14,15]. They employed critical point theory (i.e., local streamlines have indeterminate slope) to relate the invariants of the velocity-gradient tensor to the local three-dimensional flow field as seen by an observer traveling with the flow.

For completeness of the present work, and to introduce the notation utilized, the subsections below summarize the theoretical framework of the tensor-invariant based flow topology classification developed and comprehensively presented by Perry, Chong, and Cantwell [14,15]. The averaging methodology proposed to compute statistical quantities conditioned on distance from two-phase interfaces is described in Sec. III C.

A. Invariants of the velocity-gradient tensor

The velocity-gradient tensor $A_{ij} \equiv \partial u_i/\partial x_j$ can be decomposed into symmetric and skew-symmetric parts. The symmetric part is the rate-of-strain tensor

$$S_{ij} \equiv \frac{1}{2}\left(\frac{\partial u_i}{\partial x_j} + \frac{\partial u_j}{\partial x_i}\right), \tag{1}$$

and the skew-symmetric part is the rate-of-rotation tensor

$$\Omega_{ij} \equiv \frac{1}{2}\left(\frac{\partial u_i}{\partial x_j} - \frac{\partial u_j}{\partial x_i}\right), \tag{2}$$

such that $A_{ij} = S_{ij} + \Omega_{ij}$.

The coefficients (P_A, Q_A, R_A) multiplying the eigenvalues λ_i of the characteristic equation of A_{ij}, written in the form

$$\lambda_i^3 + P_A\lambda_i^2 + Q_A\lambda_i + R_A = 0, \tag{3}$$

are the tensor invariants, which, for incompressible flow ($\partial u_i/\partial x_i = 0$), are given by

$$P_A = -\mathrm{tr}(\mathbf{A}) = -A_{ii} = -(S_{ii} + \Omega_{ii}) = 0, \tag{4}$$

$$Q_A = -\tfrac{1}{2}\mathrm{tr}(\mathbf{A}^2) = -\tfrac{1}{2}A_{ij}A_{ji} = -\tfrac{1}{2}(S_{ij}S_{ji} + \Omega_{ij}\Omega_{ji}), \tag{5}$$

$$R_A = -\tfrac{1}{3}\mathrm{tr}(\mathbf{A}^3) = -\tfrac{1}{3}A_{ij}A_{jk}A_{ki} = -\tfrac{1}{3}(S_{ij}S_{jk}S_{ki} + 3\Omega_{ij}\Omega_{jk}S_{ki}). \tag{6}$$

The topological features of the velocity-gradient tensor for an incompressible flow as a function of position in (Q_A, R_A) space can be classified according to the value of the discriminant

$$D_A = \tfrac{27}{4}R_A^2 + Q_A^3, \tag{7}$$

which determines the real/imaginary nature of the eigenvalues of A_{ij}. As illustrated in Fig. 1(a), a positive discriminant, $D_A > 0$, corresponds to one real and two complex-conjugate eigenvalues (enstrophy prevalence); a negative discriminant, $D_A < 0$, gives raise to three real, distinct eigenvalues (dissipation prevalence); and a zero-valued discriminant, $D_A = 0$, corresponding to the lines $R_A = \pm(2\sqrt{3}/9)(-Q_A)^{3/2}$, indicate three real eigenvalues of which two are equal. A further classification can be made according to the sign of R_A. On the left half of the (Q_A, R_A) plane the

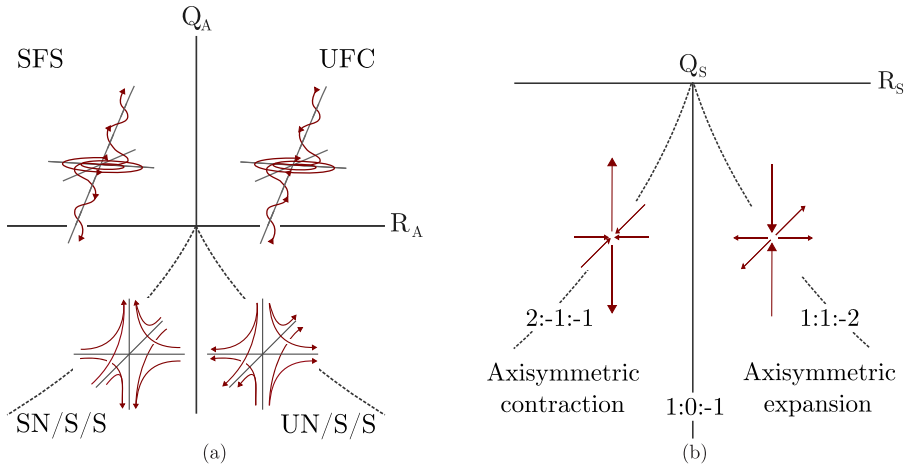

FIG. 1. Topological classification of local flow fields (streamlines) for an observer traveling with the flow on the R_A versus Q_A diagram (a): upper-left, stable focus/stretching (SFS); upper right, unstable focus/compressing (UFC); lower left, stable node/saddle/saddle (SN/S/S); lower right, unstable node/saddle/saddle (UN/S/S). Lines in (R_S, Q_S)-space corresponding to different ratios of principal strains $\lambda_1 : \lambda_2 : \lambda_3$ (b): $2 : -1 : -1$, axisymmetric contraction; $1 : 0 : -1$, two-dimensional straining limit; $1 : 1 : -2$, axisymmetric expansion.

real parts of the complex-conjugate eigenvalues are negative and the critical points of the flow are classified as stable, while on the right half-plane the real part of the eigenvalues are positive and the critical points are classified as unstable. The physical interpretation of R_A depends on the sign of D_A. One the one hand, if $D_A > 0$, $R_A < 0$ implies a predominance of vortex stretching over vortex compression (the opposite is true for $R_A > 0$). On the other hand, if $D_A < 0$, $R_A > 0$ is associated with converging flow trajectories, whereas $R_A < 0$ is connected to diverging flow trajectories. Following Chong *et al.* [15] terminology, critical point topologies falling in the upper left(right) region are called stable(unstable) focus/stretching(compressing), and those in the lower left(right) region are referred to as stable(unstable) node/saddle/saddle.

B. Invariants of the rate-of-strain and rate-of-rotation tensors

The local topology of any second-order tensor field, such as S_{ij} and Ω_{ij}, can be classified as described above, which leads to $P_S = P_\Omega = 0$ due to incompressibility, and $R_\Omega = -\det(\Omega_{ij}) = 0$ due to Ω_{ij} being skew-symmetric.

Owing to the symmetry of S_{ij}, all eigenvalues are real. Hence, only classifications for which $D_S = (27/4)R_S^2 + Q_S^3 \leqslant 0$ can be obtained on the (R_S, Q_S)-plane as shown in Fig. 1(b). In particular, all (Q_r, R_S) pairs must fall below the lines corresponding to the eigenvalue ratios (eigenvalues of S_{ij} λ_1, λ_2, λ_3 in descending order) $2 : -1 : -1$ (axisymmetric contraction) and $1 : 1 : -2$ (axisymmetric expansion). The ratio $1 : 0 : -1$ corresponds to the two-dimensional straining limit. Note also that the local dissipation rate of TKE, ε', and enstrophy, ω', can be expressed in terms of Q_S and Q_Ω as $\varepsilon' \equiv 2\nu S_{ij}S_{ij} = -4\nu Q_S$ and $\omega' \equiv 2\Omega_{ij}\Omega_{ij} = 4Q_\Omega$, respectively, with ν the kinematic viscosity of the fluid. Therefore, regions corresponding to large negative values of Q_S are sites of high dissipation, while large values of Q_Ω indicate flow regions characterized by high vorticity.

In addition, the second invariant of A_{ij}, $Q_A = Q_S + Q_\Omega$, is a measure of the relative importance of the straining and rotational parts of the velocity-gradient tensor. Regions of the flow in which Q_A is large and positive, vorticity is high and dominates the strain rate, while the reverse is true if Q_A is large and negative. This relative importance can be directly visualized by plotting Q_Ω against $-Q_S$. Points which lie near the Q_Ω-axis are in the nearly pure solid-body rotation, whereas points which

TABLE I. Flow parameters (dimensionless) at initial time ($t = 0$), droplet release time ($t = 1$), time at which tensor invariants are computed ($t = 2.5$), and final time ($t = 6$) in case A.

t	$U_{\rm rms}$	ε	ℓ	λ	η	Re_ℓ	Re_λ	ℓ/η	τ_ℓ	τ_λ	τ_η
0.0	0.0509	1.15×10^{-3}	0.0965	0.0229	1.35×10^{-3}	316	75.0	71.7	1.89	0.45	0.116
1.0	0.0457	6.10×10^{-4}	0.1038	0.0283	1.58×10^{-3}	305	83.1	65.8	2.27	0.62	0.160
2.5	0.0397	4.49×10^{-4}	0.1030	0.0286	1.70×10^{-3}	262	72.3	60.5	2.60	0.72	0.186
6.0	0.0285	2.18×10^{-4}	0.1082	0.0295	2.04×10^{-3}	198	54.0	53.0	3.80	1.04	0.268

lie near the $-Q_S$-axis have nearly pure straining motions. Points around the 45° line, where strain rate and rotation are of the same order, correspond to regions of the flow dominated by sheet-like motions, like those found in boundary layers [16].

III. NUMERICAL SIMULATION AND FLOW PROPERTIES

This study uses results from DNS of droplet-laden decaying HIT [3]. These simulations used the volume-of-fluid (VoF) method to resolve the flow inside and outside the droplets and modeled surface tension effects. A full description of the numerical methods that were used to simulate this flow is offered by Refs. [25,26].

A. Initial conditions and droplet properties

Table I shows the dimensionless flow parameters at different times t for the droplet-free flow (case A): ℓ and τ_ℓ are the integral length and timescales; Re_ℓ is the Reynolds number based on ℓ; λ is the Taylor length scale; and η and τ_η are the Kolmogorov length and timescales. The initial turbulent flow field is well-resolved, as indicated by $\kappa_{\max}\eta = 4.3$ at $t = 0$, where $\kappa_{\max} = \pi N$ is the maximum resolved wave number and $N = 1024$ is the number of grid points in each direction of the computational grid.

The dataset contains one simulation (case A) of droplet-free flow and eight simulations (A⋆–H) of droplet-laden isotropic turbulence (Table II). Case A⋆ is a limiting case in which the viscosity and density ratio are unity and the Weber number of the droplets is infinity. We analyze the effects of varying the initial droplet Weber number ($\mathrm{We}_{\rm rms} = D_0 U_{\rm rms}^2 \rho_c/\sigma$), where σ is the surface tension coefficient, droplet- to carrier-fluid density ratio ($\varphi = \rho_d/\rho_c$), and droplet- to carrier-fluid viscosity ratio ($\gamma = \mu_d/\mu_c$) in the three sets BCD, CEF, and CGH, respectively, while keeping the other two parameters constant. In cases B, C, and D, $\mathrm{We}_{\rm rms}$ increases from 0.1 to 5.0 by decreasing the surface tension coefficient. In cases C, E, and F, φ increases from 1 to 100 by increasing ρ_d. In cases C, G, and H, γ increases from 1 to 100 by increasing μ_d. For all cases, the droplet volume

TABLE II. Droplet properties (dimensionless) at release time ($t = 1$).

Case	$\mathrm{We}_{\rm rms}$	$\varphi \equiv \rho_d/\rho_c$	$\gamma \equiv \mu_d/\mu_c$	τ_d	τ_d/τ_ℓ	τ_d/τ_η	ϕ_m	ϕ_v	We
A	—	—	—	—	—	—	0	0	—
A⋆	∞	1	1	—	—	—	0.05	0.05	∞
B	0.1	10	10	35.9	15.8	225	0.5	0.05	1.53×10^3
C	1.0	10	10	35.9	15.8	225	0.5	0.05	1.53×10^4
D	5.0	10	10	35.9	15.8	225	0.5	0.05	7.65×10^4
E	1.0	1	10	3.59	1.58	22.5	0.05	0.05	1.53×10^4
F	1.0	100	10	359	158	2250	5.0	0.05	1.53×10^4
G	1.0	10	1	41.8	18.4	261	0.5	0.05	1.53×10^4
H	1.0	10	100	34.9	15.4	219	0.5	0.05	1.53×10^4

fraction is $\alpha_v = 0.05$, the initial number of droplets is $N_d = 3130$, and the initial nondimensional droplet diameter is $D_0 = 0.03125$, which is $20\eta_1$ (or $1.1\lambda_1$), where η_1 and λ_1 are the Kolmogorov and Taylor length scales, respectively, at the time the droplets are released in the flow ($t = 1$). This yields a droplet resolution of 32 grid points per diameter ($N_{\mathrm{gp,d}} = 32$). We will first focus on case C as a base scenario and subsequently analyze the effects of varying $\mathrm{We}_{\mathrm{rms}}$, φ, and γ on the velocity-gradient invariants.

B. Length scales of droplet-laden isotropic turbulence

In single-phase isotropic turbulence, η characterizes the smallest length scales of the flow. Whether this still holds in isotropic turbulence laden with finite-size droplets depends on the flow and droplet properties. If droplet breakup and coalescence are considered, then thin ligaments and gas films are almost always several orders of magnitude smaller than the smallest length scales of the surrounding flow, and therefore expected to be much smaller than η. In the present flow, breakup events are limited by keeping the Weber number order unity and coalescence events are minimized by setting the droplet volume fraction to a relatively low value (5%).

The other length scale that could be smaller than η is the one associated with the velocity gradients that develop at the interface between the droplet and carrier fluid. We can obtain a conservative estimate of the thickness of this transition region in which viscous effects dominate if we assume its thickness to be equal to the thickness of the boundary layer on a rigid sphere immersed in a uniform flow. This estimate is conservative because, compared to rigid spheres, droplets develop internal circulation in the direction of the free-stream flow, which effectively lowers the free-stream velocity (U_∞) and thus increases the boundary-layer thickness.

To estimate the nominal boundary-layer thickness of the droplet, we model the droplet as a rigid sphere in uniform flow. The free-stream velocity seen by the droplet is taken as the r.m.s. velocity of the surrounding turbulent flow. This approximation is reasonable given that the droplet diameter is roughly three times smaller than the integral scale of turbulence ($\ell/D_0 = 3.3$); therefore, the energy-containing scales, as experienced by the droplet, are relatively large compared to its size. We find an approximate laminar boundary-layer solution for the sphere by numerically solving the momentum integral equation for arbitrarily varying free-stream velocity over a body of revolution. Using U_{rms} at $t = 2.5$ as the free-stream velocity ($U_\infty = 0.0397$ and $\mathrm{Re}_D = U_\infty D_0/\nu = 80$), which corresponds to roughly one integral timescale after droplet release, the calculated nondimensional boundary-layer thickness at the forward stagnation point ($\theta = 0$, where the boundary layer is thinnest) is $\delta_{99} = 0.0036$, and near the separation point ($\theta = 90^\circ$) it is $\delta_{99} = 0.0068$. The average nondimensional boundary-layer thickness over the leading surface is $\bar{\delta}_{99} = 0.0044$, which, in terms of the initial droplet diameter, gives $D_0/\bar{\delta}_{99} = 7.1$. This value for $\bar{\delta}_{99}$ should be taken as a rough estimate of the mean boundary-layer thickness on the droplets since we are neglecting droplet shape effects, nonuniform and unsteady flow effects, and droplet internal circulation. Nevertheless, the DNS results will show that $\bar{\delta}_{99}$ accurately demarcates the transition from boundary-layer-like flow topologies to those characteristic of HIT.

C. Conditional averaging methodology

Motivated by isolating the flow topologies near the droplet surface, we introduce a conditional averaging procedure to compute statistical quantities conditioned on distance from the interface. Starting with the VoF field, we use the marching cubes algorithm [27] to compute a level set (LS), or signed distance function, representing the shortest distance to the interface, which has the property $\phi = 0$ at the interface, $\phi < 0$ in the droplet fluid, and $\phi > 0$ in the carrier fluid. Figure 2 shows the VoF and LS fields in an x-y plane at the time when the tensor invariants are computed ($t = 2.5$). Note that the computational cost of our algorithm to compute ϕ for a given C scales as $(|\phi|_{\max}N)^3$, where $|\phi|_{\max}$ is the maximum search distance for computing ϕ and N is the number of grid points in each spatial direction. Therefore, to limit computational cost while still adequately capturing

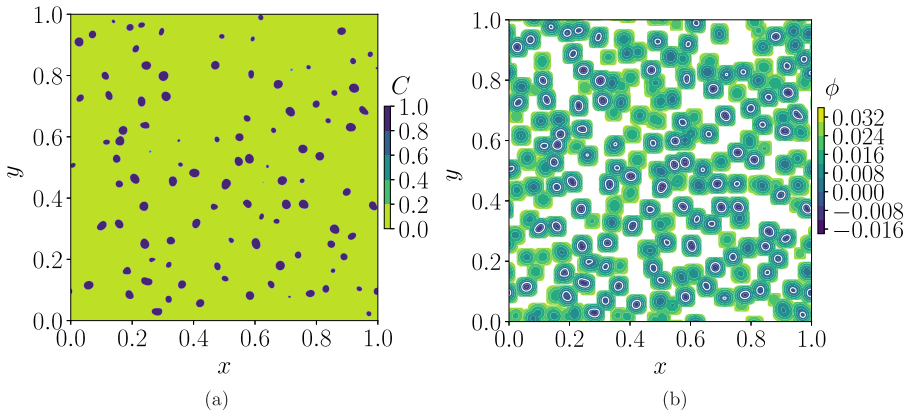

FIG. 2. Instantaneous contours in the x-y plane of (a) the VoF field, $C = C(\mathbf{x}, t)$, and (b) the level-set field, $\phi = \phi(\mathbf{x}, t)$, for case C at $t = 2.5$.

the boundary-layer region, we set $|\phi|_{\max}$ to approximately one droplet diameter D_0. This limitation explains the white regions in Fig. 2(b).

IV. RESULTS

A. Conditionally averaged dissipation rate

The introduction of finite-size droplets into HIT increases the decay rate of TKE relative to droplet-free flow [3]. By comparing the relative magnitudes of the terms in the carrier-fluid TKE budget equation

$$\frac{dk_c(t)}{dt} = -\varepsilon_c(t) + T_{v,c}(t) + T_{p,c}(t), \tag{8}$$

where $\varepsilon_c(t)$ is the dissipation rate of TKE, $T_{v,c}(t)$ is the viscous power, and $T_{p,c}(t)$ is the pressure power, DNS has shown that the enhanced decay rate of k_c is primarily caused by an increase in magnitude of ε_c. Analyzing contours of the local dissipation rate in the presence of the droplets, has qualitatively shown that the dissipation rate is enhanced near the droplet interface, explaining the increase in the magnitude of $\varepsilon_c(t)$. To quantify the enhanced dissipation of TKE near the interface, we condition $\varepsilon' \equiv \mathrm{Re}^{-1}(2\mu S_{ij}S_{ij})$ on ϕ using the method described in Sec. III C. Figure 3 shows the conditional dissipation rate, $\langle\varepsilon'|\phi\rangle$, as a function of distance from the interface, ϕ, and normalized by the dissipation rate at $t = 1$, ε_1, for all cases. When computing the conditional mean, we only include those statistics in which there are at least one million samples, which has been shown to yield statistically converged results [3]. Note that in case A* (We $= \infty$), the interface is a fluid tracer surface; therefore, as the flow evolves, the interface area increases substantially due to strain, so the probability of finding a point at some distance from the interface decreases in time. This explains, in part, why the domain of $\langle\varepsilon'|\phi\rangle$ in case A* decreases in time and is less than for the finite-Weber-number cases.

Figure 3 shows that in the droplet-laden cases (B–H), $\langle\varepsilon'|\phi\rangle$ is maximum at the interface ($\phi = 0$) for all times. In fact the dissipation rate at $\phi = 0$ on both the droplet-fluid and carrier-fluid sides of the interface is several times larger than the rate away from the interface ($|\phi/D_0| > 0.2$). In addition, in the cases of highest Weber number [case B in Fig. 3(b)] and highest viscosity ratio [case H in Fig. 3(h)], $\langle\varepsilon'|\phi\rangle$ is always an order of magnitude larger at the interface than away from the interface. Because the dissipation enhancement persists in time and is markedly higher than in case A*, it suggests that this effect is not a result of the initial condition of setting the initial droplet velocity to zero, but rather robust. The enhanced dissipation near the interface is a result of an increase

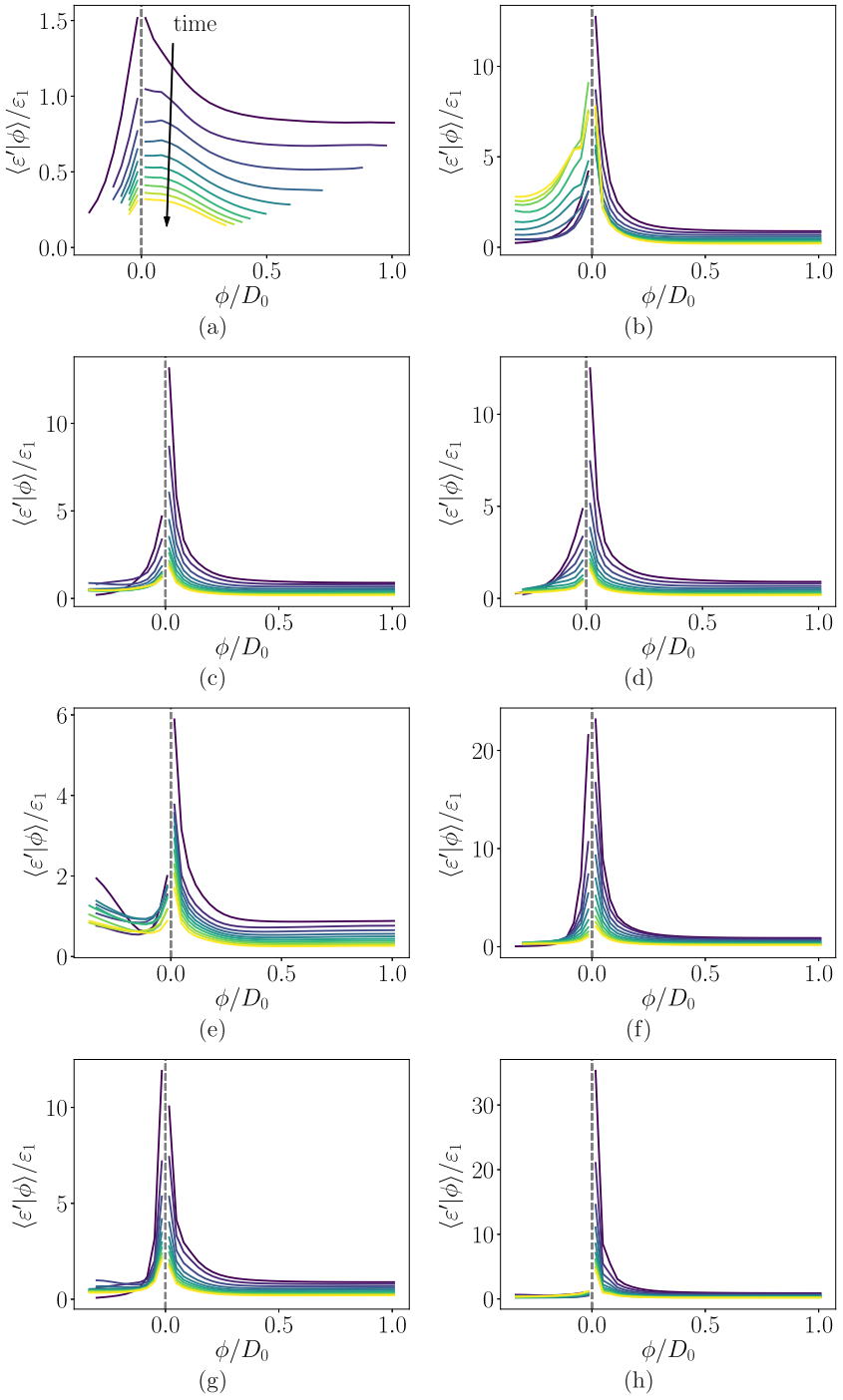

FIG. 3. Dissipation rate conditionally averaged on distance from the interface ($\langle \varepsilon' | \phi \rangle$) for (a–h) cases A* to H and various times from $t = 1$ to 6. The intensity of the line decreases as time increases as indicated in panel (a).

TABLE III. Viscous scaling parameters at $t = 2.5$: shear stress at the interface, τ_Σ, interfacial friction velocity in the carrier phase, $u_{\tau_c,\Sigma}$, viscous length scale in the carrier phase, $\delta_{\nu_c,\Sigma}$, and interfacial viscous length scale in the carrier phase normalized by the mean viscous length scale of the carrier phase $\delta_{\nu_c,\Sigma}/\delta_{\nu_c}$.

Case	τ_Σ	$u_{\tau_c,\Sigma}$	$\delta_{\nu_c,\Sigma}$	$\delta_{\nu_c,\Sigma}/\delta_{\nu_c}$
A*	4.85×10^{-5}	6.96×10^{-3}	2.24×10^{-3}	1.02
B	2.45×10^{-4}	1.57×10^{-2}	9.94×10^{-4}	0.453
C	2.41×10^{-4}	1.55×10^{-2}	1.00×10^{-3}	0.458
D	2.33×10^{-4}	1.53×10^{-2}	1.02×10^{-3}	0.465
E	1.77×10^{-4}	1.33×10^{-2}	1.17×10^{-3}	0.533
F	3.40×10^{-4}	1.84×10^{-2}	8.45×10^{-4}	0.385
G	1.40×10^{-4}	1.18×10^{-2}	1.31×10^{-3}	0.599
H	3.40×10^{-4}	1.84×10^{-2}	8.45×10^{-4}	0.386

in the velocity gradient $\partial u_i/\partial x_j$. This is caused by the droplet Stokes number based on both the Kolmogorov and integral timescales (τ_d/τ_η and τ_d/τ_ℓ) being much larger than unity; consequently, the droplet motion deviates from the carrier-fluid turbulent eddies. Due to the continuity condition that $\mathbf{u}_c = \mathbf{u}_d$ at the interface, the carrier-fluid velocity $\mathbf{u}_c$ at $\phi = 0$ is strongly influenced by the droplet motion.

B. Viscous scales

We define viscous scales that characterize the velocity scales and length scales near the droplet surface. These scales serve as (i) a measure of the smallest hydrodynamic scale at the droplet surface and (ii) a reference quantity for normalizing the velocity gradient and distance from the interface.

We first compute the mean interfacial shear stress

$$\tau_\Sigma = \langle \sqrt{(\mathbf{t}_1 \cdot 2\mu\mathbf{S} \cdot \mathbf{n})^2 + (\mathbf{t}_2 \cdot 2\mu\mathbf{S} \cdot \mathbf{n})^2} \rangle_\Sigma, \tag{9}$$

where $\mathbf{t}_1$ and $\mathbf{t}_2$ are two orthogonal unit vectors that are tangent to the droplet surface, $\mathbf{n}$ is the unit normal, and the brackets $\langle \ldots \rangle_\Sigma$ denote ensemble averaging over all computational cells containing the interface. Note that in the absence of surface tension gradients (i.e., no Marangoni stresses), the shear stress is continuous across the interface ($\tau_\Sigma = \tau_{\Sigma,c} = \tau_{\Sigma,d}$). Next, the friction velocity

$$u_{\tau_k,\Sigma} \equiv \sqrt{\frac{\tau_\Sigma}{\rho_k}} \tag{10}$$

and viscous length scale

$$\delta_{\nu_k,\Sigma} \equiv \nu_k \sqrt{\frac{\rho_k}{\tau_\Sigma}} = \frac{\nu_k}{u_{\tau_k,\Sigma}} \tag{11}$$

are defined in the same manner as for turbulent wall-bounded flows, where the subscript $k = c$ or d denotes carrier- or droplet-phase quantities, respectively. Using $\delta_{\nu_c,\Sigma}$ and $u_{\tau_c,\Sigma}$, the distance ϕ and velocity gradient tensor $\mathbf{A}$ are normalized in the carrier phase in terms of viscous units as

$$\phi^+ \equiv \frac{\phi}{\delta_{\nu_c,\Sigma}}, \quad \mathbf{A}^+ \equiv \frac{\delta_{\nu_c,\Sigma}\mathbf{A}}{u_{\tau_c,\Sigma}}. \tag{12}$$

The values of $u_{\tau_c,\Sigma}$ and $\delta_{\nu_c,\Sigma}$ are reported in Table III for all cases.

A fundamental question we aim to address is how does $\delta_{\nu_c,\Sigma}$ compare to the smallest length scale of the surrounding turbulent flow, the Kolmogorov scale of the carrier phase η_c. To make the

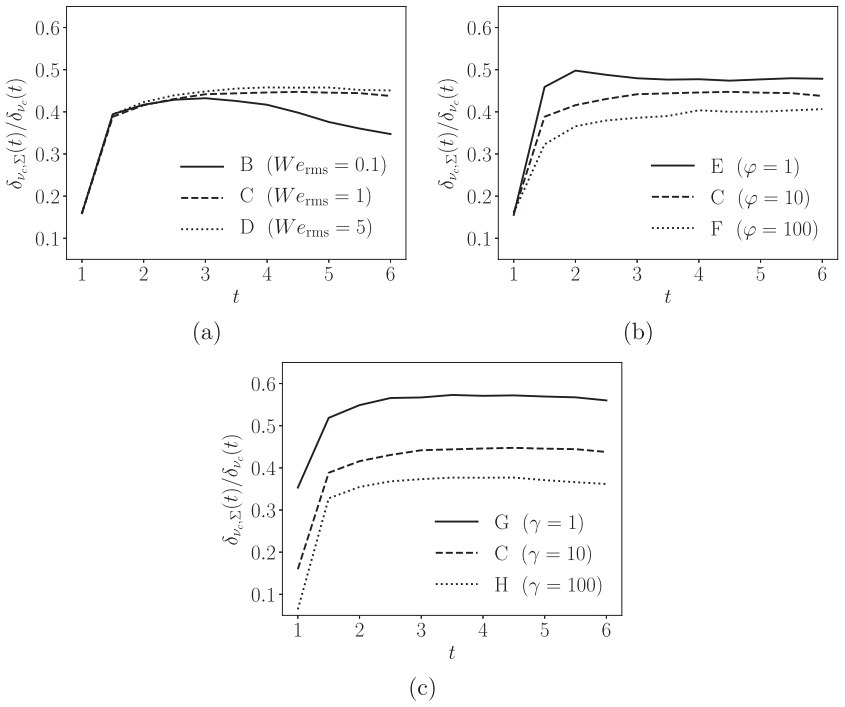

FIG. 4. Time evolution of the interfacial viscous length scale in the carrier phase $\delta_{\nu_c,\Sigma}(t)$ normalized by the mean viscous length scale of the carrier phase $\delta_{\nu,c}(t)$ for varying (a) Weber number, (b) density ratio, and (c) viscosity ratio.

comparison direct, we compute the viscous length scale of the carrier phase

$$\delta_{\nu_c} = \nu_c \sqrt{\frac{\rho_c}{\tau_c}}, \tag{13}$$

where the mean shear stress for canonical decaying isotropic turbulence is

$$\tau_c = \mu_c \sqrt{\frac{4\varepsilon_c}{15\nu_c}}. \tag{14}$$

Note that, in this context, δ_{ν_c} is simply an alternative definition of the Kolmogorov microscale. The relationship between δ_ν and η is $\delta_\nu = (15/4)^{1/4}\eta \approx 1.39\eta$.

Table III shows that $\delta_{\nu_c,\Sigma}/\delta_{\nu_c}$ in case A* is close to unity as would be expected for canonical decaying HIT which indicates that the effect of initial conditions is undetectable at $t = 2.5$. If we compare $\delta_{\nu,c}/\delta_{\nu_c}$ for case A* to the droplet-laden cases B–H, $\delta_{\nu,c}/\delta_{\nu_c}$ for the droplet-laden cases is consistently two to three times smaller. Figure 4 shows the time evolution of $\delta_{\nu_c,\Sigma}$ normalized by $\delta_{\nu,c}$. For all cases and all times, $\delta_{\nu,c}/\delta_{\nu_c}$ is less than unity, therefore the smallest length scale is always located at the droplet surface due to the induced velocity gradient. Looking at the time evolution of $\delta_{\nu,c}/\delta_{\nu_c}$, we recall that the droplets are released from rest at $t = 1$, leading to an instantaneous increase in τ_Σ which explains the minimum in $\delta_{\nu_c,\Sigma}/\delta_{\nu_c}$. However, after roughly one integral timescale ($t \geqslant 1 + \tau_\ell \approx 2.8$), $\delta_{\nu_c,\Sigma}/\delta_{\nu_c}$ reaches a quasistationary value, which suggests that the effect of the initial conditions is forgotten after one integral timescale.

The effects of varying $\mathrm{We}_{\rm rms}$, φ, and γ on $\delta_{\nu_c,\Sigma}$ are as follows. Figure 4(a) shows that as $\mathrm{We}_{\rm rms}$ increases $\delta_{\nu_c,\Sigma}/\delta_{\nu_c}$ increases. The decrease in $\delta_{\nu_c,\Sigma}/\delta_{\nu_c}$ for case B at later times is explained by droplet coalescence. Droplet coalescence produces velocity fluctuations (TKE) at the droplet scale

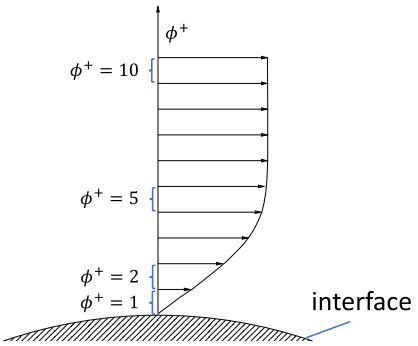

FIG. 5. Schematic illustrating the layers near the droplet interface used for conditional averaging.

through the power of the surface tension Ψ_σ, and because the interfacial surface energy scales as We^{-1}, the effect is most pronounced for the lowest Weber number case B ($\mathrm{We}_{\mathrm{rms}} = 0.1$). As the density ratio increases, shown in Fig. 4(b), $\delta_{\nu_c,\Sigma}/\delta_{\nu_c}$ decreases, showing that higher inertia droplets have larger velocity gradients and smaller length scales near their surfaces than lighter droplets. Figure 4(c) shows that increasing the viscosity ratio γ leads to a decrease in $\delta_{\nu_c,\Sigma}/\delta_{\nu_c}$. This suggests that in the solid particle limit ($\gamma \to \infty$), $\delta_{\nu_c,\Sigma}/\delta_{\nu_c}$ would be minimum. This implies that, from a computational perspective, solid particles are the most costly dispersed medium to simulate in terms of resolving the velocity gradient near the particle surface.

After one integral timescale, $\delta_{\nu_c,\Sigma}/\delta_{\nu_c}$ ranges between 0.35 and 0.5 depending on the case, indicating that $\delta_{\nu_c,\Sigma}$ is two to three times smaller than the smallest length scale in the surrounding turbulent flow. Consequently, to perform fully resolved DNS of droplet-laden flows (ignoring breakup and coalescence for the time being), there is an additional microscale that must be resolved that is significantly smaller than the Kolmogorov scale. For the cases considered here, the number of grid points required on a fixed mesh is roughly eight to twenty-seven (2^3–3^3) times higher than single-phase isotropic turbulence at an identical Reynolds number. This fact, in part, explains why a numerical resolution of $\kappa_{\max}\eta = 4.3$ was used to produce this DNS dataset.

C. Joint PDFs of tensor invariants

1. Effect of distance from the interface

In this section we present the invariants of the velocity-gradient tensor in the carrier fluid for case C and investigate how the topology of the turbulence changes as the droplet interface is approached. The tensor invariants are computed at every point in the flow using second-order central differences, except near the interface, where the central difference stencil would lead to mixing droplet- and carrier-fluid velocities. In that scenario, a second-order one-sided scheme is used.

The joint PDFs are computed in four different layers on the basis of the distance from the interface at $0 \leqslant \phi^+ \leqslant 1$, $1 \leqslant \phi^+ \leqslant 2$, $4 \leqslant \phi^+ \leqslant 5$, and $9 \leqslant \phi^+ \leqslant 10$, which we will term the $\phi^+ = 1$, 2, 5, and 10 layers, respectively. These layers are represented schematically in Fig. 5. The approximate mean boundary layer thickness in viscous units at $t = 2.5$ is $\bar{\delta}^+_{99} = 4.4$, and therefore the $\phi^+ = 10$ is outside the boundary layer, $\phi^+ = 5$ is at the edge of the boundary layer and $\phi^+ = 2$ and $\phi^+ = 1$ are inside the boundary layer. Figure 6 shows the joint PDFs of Q_A^+ versus R_A^+, Q_S^+ versus R_S^+, and $-Q_S^+$ versus Q_Ω^+ conditionally averaged on the different layers. The joint PDF of Q_A^+ versus R_A^+ in the $\phi^+ = 10$ layer shows that the most probable flow topologies are in the upper left ($Q_A^+ > 0$ and $R_A^+ < 0$) and lower right ($Q_A^+ < 0$ and $R_A^+ > 0$) quadrants, indicating that the most likely flow topologies are stable focus/stretching and unstable node/saddle/saddle. As a reminder, topologies corresponding to ($Q_A^+ > 0$ and $R_A^+ < 0$) represent high enstrophy, vortical motions that contribute to the production of enstrophy via vortex stretching. When $Q_A^+ < 0$ and $R_A^+ > 0$, this is

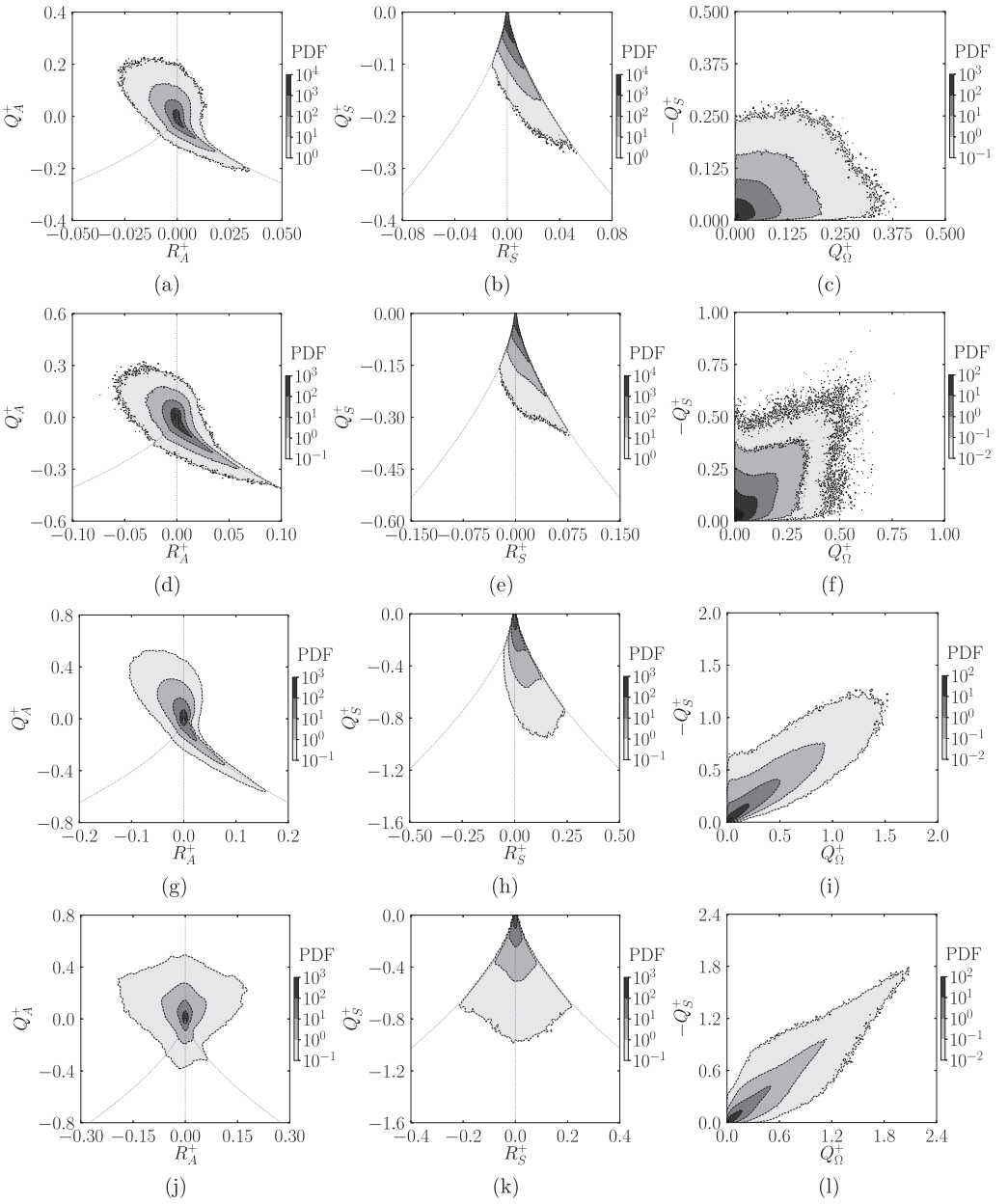

FIG. 6. Joint PDFs of (a, d, g, j) Q_A^+ versus R_A^+, (b, e, h, k) Q_S^+ versus R_S^+, and (c, f, i, l) $-Q_S^+$ versus Q_Ω^+ for case C conditioned on different distances from the interface: (a–c) $\phi^+ = 10$, (d–f) $\phi^+ = 5$, (g–i) $\phi^+ = 2$, and (j–l) $\phi^+ = 1$.

indicative of regions of high strain/dissipation that are undergoing compression in one direction and extension in the two other directions (biaxial strain). The particularly inclined teardrop shape, the clustering along the so-called Vieillefosse tail in the lower right quadrant, and self-similarity of the joint PDF shown in Fig. 6(a) closely resemble those found in single-phase HIT [28] as well as various inhomogeneous turbulent flows [16,19,29]. This suggests that for $\phi^+ > \bar{\delta}_{99}^+$, the small-scale

motions closely follow the universal properties of single-phase turbulence and that the modulation of turbulence by the droplets is undetected by looking at the fine-scale motions.

The sequence of Figs. 6(a), 6(d), 6(g), and 6(j), shows the joint PDFs of Q_A^+ versus R_A^+ as the interface is approached. By comparing lines of constant probability density, the results show that the magnitudes of Q_A^+ and R_A^+ increase monotonically from the layers at $\phi^+ = 10$ to $\phi^+ = 1$, meaning that, on average, the magnitude of the velocity gradients increases as the interface is approached. This is consistent with the droplets' inertia causing their trajectories to deviate from the carrier fluid and leading to increased velocity gradients. For $\phi^+ = 1$, the shape of the joint PDFs departs from teardrop and becomes more symmetric with respect to the R_A^+-axis, presenting the highest probabilities at $Q_A^+ = 0$ and $R_A^+ = 0$.

Events clustered at $Q_A = 0$ and $R_A = 0$ are indicative of boundary-layer-like flow topologies [19]. To see this, consider A_{ij} in a planar boundary-layer flow. Without loss of generality, the interface is oriented such that the interface normal is aligned with the y axis and the velocity is aligned with the x axis, such that at the droplet surface the velocity-gradient tensor, to leading order [30], is

$$A_{ij} = \begin{bmatrix} 0 & \partial u/\partial y & 0 \\ 0 & 0 & 0 \\ 0 & 0 & 0 \end{bmatrix}. \tag{15}$$

The invariants of Eq. (15) are $Q_A = R_A = 0$, $Q_S = (\partial u/\partial y)^2/4$, $R_S = 0$, and $Q_\Omega = -Q_S$. It is perhaps not surprising then that the symmetry about the R_A^+-axis and clustering near the origin were also reported in turbulent channel flow [19].

Figures 6(b), 6(e), 6(h), and 6(k) show the joint PDFs of Q_S^+ versus R_S^+ for the four layers near the interface. Farthest from the interface and outside the droplet boundary layer ($\phi^+ = 10$), Fig. 6(b) shows that the PDF is skewed toward $R_S^+ > 0$, with most of the events attracted to the line $27R_S^2 + 4Q_S^3 = 0$. Along this line, the principal rates of strain are in the ratio $\lambda_1 : \lambda_2 : \lambda_3 = 1 : 1 : -2$; therefore, the flow is expanding in two directions and contracting in the third direction, forming disk-like structures. A comparison of Figs. 6(b), 6(e), 6(h), and 6(k), show that as ϕ decreases the flow becomes less skewed toward the biaxial straining topologies. At the droplet interface, there is equal probability of finding biaxial ($R_S^+ > 0$) and axial ($R_S^+ < 0$) strain fields, and the most likely events appear to lie along the line $R_S^+ = 0$. The clustering along $R_S^+ = 0$ is consistent with the invariants for $\mathbf{A}$ in a planar boundary layer as shown in Eq. (15). The increasing preference for $R_S^+ = 0$ events as the interface is approached is also in agreement with the behavior of Q_S and R_S reported in turbulent channel flow [19] as the distance to the wall decreases.

We now look at the joint PDFs of Q_S^+ and Q_Ω^+ shown in Figs. 6(c), 6(f), 6(i), and 6(l). At the distance farthest from the droplet surface ($\phi^+ = 10$), shown in Fig. 6(c), the PDF is skewed toward small-scale motions with low dissipation and high enstrophy ($Q_\Omega^+ > -Q_S^+$). This is explained by the fact that motions with high enstrophy are solid-body rotations and, therefore, persist for a longer time than unstable straining motions [28]. The shape of the joint PDF in Fig. 6(c) is in good agreement with that found in single-phase isotropic turbulence. As ϕ decreases, the magnitude of the invariants increases by nearly an order of magnitude, indicating that both the mean enstrophy and dissipation rate increase substantially as the droplet surface is approached. Interestingly, as ϕ^+ changes from 10 to 5 in Figs. 6(c) and 6(f), the PDF goes from being skewed toward $Q_S^+ = 0$ to $Q_\Omega^+ = 0$. This signals that outside the boundary layer, there is a preference for vortical motions, as previously mentioned, but at the edge of the droplet boundary layer, more dissipative flow topologies are prevailing.

Moving into the boundary layer from $\phi^+ = 5$ to $\phi^+ = 2$ and 1, shown in Figs. 6(i) and 6(l), the distribution of Q_S^+ and Q_Ω^+ clusters along the line $Q_\Omega = -Q_S$, corresponding to vortex sheet structures. This preference for $Q_\Omega = -Q_S$ is explained by Eq. (15) and was also observed in the buffer and viscous regions of a turbulent boundary layer [19]. Figure 7 shows instantaneous two-dimensional contours of $-Q_S^+ + Q_\Omega^+$ in a subregion of the computational domain at $t = 2.5$ in case

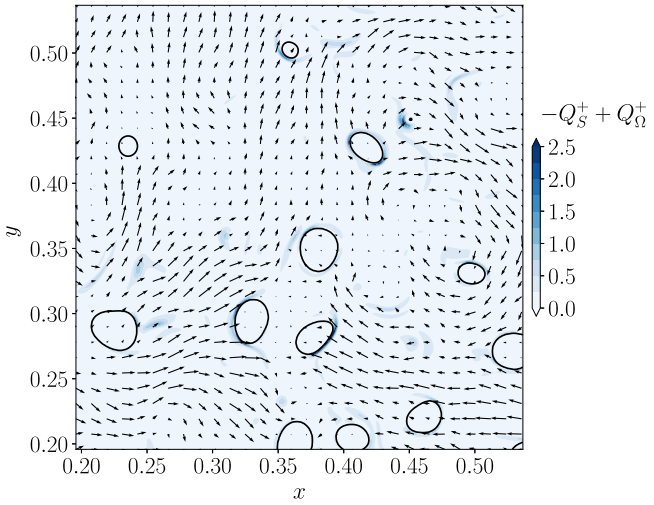

FIG. 7. Instantaneous contours in a subregion of the x-y plane of $-Q_S^+ + Q_\Omega^+$ ($= A_{ij}A_{ij}/2$) for case C at $t = 2.5$. The droplet interface is marked by a black line and the velocity vectors are projected onto the x-y plane at every 12th grid point.

C. We observe dark blue regions on the windward side of some of the droplets where both the dissipation rate and enstrophy are high, which is characteristic of vortex sheet topologies. Values of $-Q_S^+ + Q_\Omega^+ \approx 2.5$ correspond to the more rare/extreme events shown in the joint PDFs of Figs. 6(i) and 6(l) (e.g., events where $-Q_S^+ \approx Q_\Omega^+ \approx 1.25$).

2. *Weber number effects*

As the droplet Weber number increases (cases B–D), the surface tension forces decrease relative to the aerodynamic forces on the droplet surface, which leads to larger droplet deformations. The fact that the droplet is freer to undergo larger deformations has a relieving effect and causes the interfacial shear stress τ_Σ to decrease by 5% with increasing $\mathrm{We}_{\mathrm{rms}}$ as shown in Table III. The effects of increasing $\mathrm{We}_{\mathrm{rms}}$ on the invariants Q_A, R_A, Q_S, R_S, and Q_Ω conditioned on $\phi^+ = 1$ are shown in Fig. 8.

The sequence of panels in Figs. 8(a)–8(c) shows that increasing $\mathrm{We}_{\mathrm{rms}}$ does not have a strong effect on the Q_A and R_A invariants. In all cases, there is clustering near the origin. There is a slight trend for increasing probability of events along the line $R_A^+ = 0$ and for $Q_A^+ > 0$ with large Q_A^+ values becoming more likely as $\mathrm{We}_{\mathrm{rms}}$ increases. $R_A^+ = 0$ and $Q^+ > 0$ correspond to two purely imaginary eigenvalues and one eigenvalue being zero. Physically, this denotes a flow field undergoing solid body rotation [e.g., $(u, v, w) = (-y, x, 0)$]. The similarity among the joint PDFs of Q_S versus R_S in Figs. 8(d)–8(f), indicates that increasing $\mathrm{We}_{\mathrm{rms}}$ has a negligible effect on modifying the topology of the strain field. The PDFs of $-Q_S^+$ versus Q_Ω^+ shown in Figs. 8(g)–8(i) indicate that the probability of vortex sheet topologies ($-Q_S^+ = Q_\Omega^+$) decreases with increasing $\mathrm{We}_{\mathrm{rms}}$. For the most deformable $\mathrm{We}_{\mathrm{rms}} = 5$ droplets, Fig. 8(i) shows that the PDF is skewed towards higher enstrophy topologies. This suggests that more spherical droplets (lower $\mathrm{We}_{\mathrm{rms}}$) promote the formation of vortex sheet topologies.

3. *Density ratio effects*

In this section we analyze cases E, C, and F, in which the density ratio between the droplet and carrier fluid is increased as $\varphi = 1$, 10, and 100, respectively, by increasing the density of the droplet fluid. This increases the droplet inertia and thereby increases its response time to changes in the

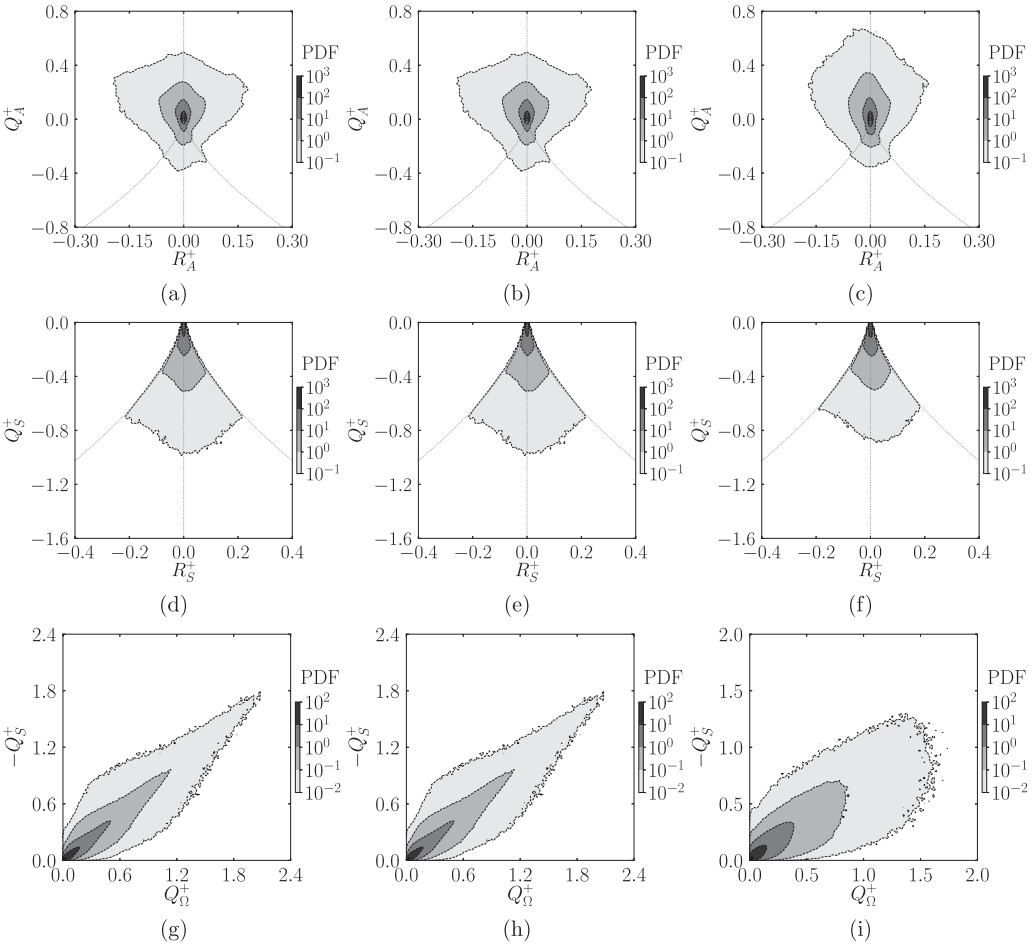

FIG. 8. Joint PDFs of (a–c) Q_A^+ versus R_A^+, (d–f) Q_S^+ versus R_S^+, and (g–h) $-Q_S^+$ versus Q_Ω^+ for cases of increasing Weber number $\mathrm{We}_{\mathrm{rms}} =$ (a, d, g) 0.1, (b, e, h) 1, and (c, f, i) 5 (cases B–D) conditioned on $\phi^+ = 1$.

surrounding fluid flow, which, consequently, leads to larger velocity differences between the droplet and carrier fluid. Table III shows that as the density ratio increases from 1 to 100, τ_Σ nearly doubles in magnitude, which is associated with a significant decrease in $\delta_{v_c,\Sigma}$.

Figure 9 shows the joint PDFs of the invariants for varying φ. The Q_A^+ and R_A^+ invariants, as shown in Figs. 9(a)–9(c), indicate that for unity density ratio, the distribution shows some resemblance to the canonical teardrop shape of HIT, especially with unstable node saddle/saddle topologies favored, but as the density ratio increases, the distribution becomes symmetric with respect to the R_A^+ axis. Looking at the rate-of-strain invariants, Figs. 9(g)–9(i), it is observed that as φ increases, the probability of finding vortex sheet topologies increases. At unity density ratio, a broader distribution of $-Q_S^+$ and Q_Ω^+ invariants is shown with a shift in preference for vortex sheets to vortex tubes.

4. Viscosity ratio effects

The viscosity ratio between the droplet and carrier fluid is augmented by increasing the viscosity of the droplet fluid. In cases G, C, and H, $\gamma = 1$, 10, and 100, respectively. The effect of increasing

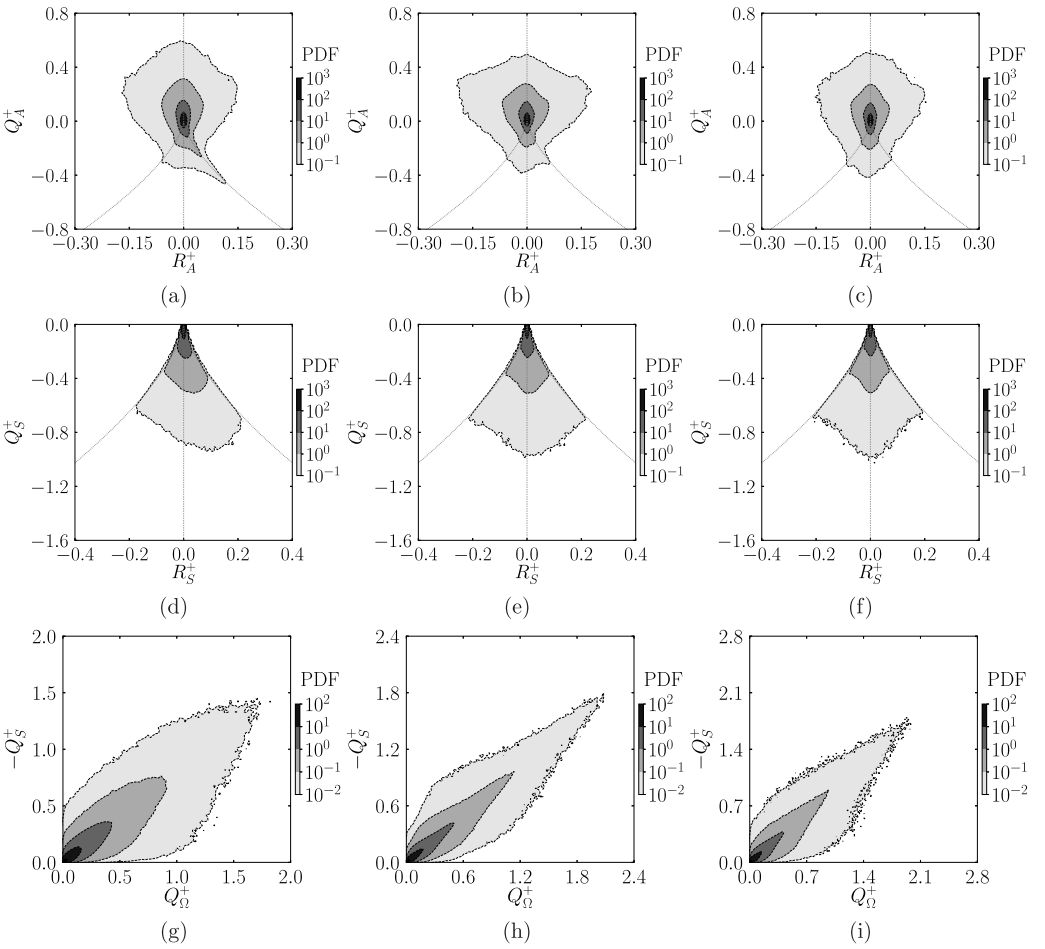

FIG. 9. Joint PDFs of (a–c) Q_A^+ versus R_A^+, (d–f) Q_S^+ versus R_S^+, and (g–h) $-Q_S^+$ versus Q_Ω^+ for cases of increasing density ratio $\varphi =$ (a,d,g) 1, (b, e, h) 10, and (c, f, i) 100 (cases E, C, F) conditioned on $\phi^+ = 1$.

γ on the the interfacial shear stress is pronounced; Table III shows that as γ increases from 1 to 100, τ_Σ increases by 140%. As γ increases, the velocity gradient in the carrier phase increases while that in the droplet phase decreases. This physical mechanism is described in greater detail in Ref. [3].

Figure 10 shows the joint PDFs of the A_{ij}, S_{ij}, and Ω_{ij} invariants for increasing γ conditioned on $\phi^+ = 1$. The PDFs of the velocity gradient invariants, shown in Figs. 10(a)–10(c), indicate that for low viscosity ratio ($\gamma = 1$), vortical motions ($Q_A^+ > 0$) are preferred, but for the highest viscosity ratio ($\gamma = 100$), strain-dominated flow topologies are favored. It is interesting to note that for $\gamma = 100$, the rate-of-strain invariants, as shown in Fig. 10(f), show an equal preference for axisymmetric contraction and axisymmetric expansion. The shift from enstrophy- to strain-dominated topologies is also clear in the joint PDFs of $-Q_S^+$ and Q_Ω^+ [Figs. 10(g)–10(i)]. For $\gamma = 1$, the PDF is skewed towards the Q_Ω^+ axis indicating a preference for topologies associated with low strain and high vorticity. The emergence of structures along the 45° line for $\gamma = 10$ is indicative of vortex sheet topologies. At the highest viscosity ratio tested, $\gamma = 100$, there is an even more pronounced preference for vortex sheet topologies, and, interestingly, there also emerges a secondary structure in the vertical direction that denotes irrotational dissipation ($-Q_S^+ > 0$ and $Q_\Omega^+ = 0$).

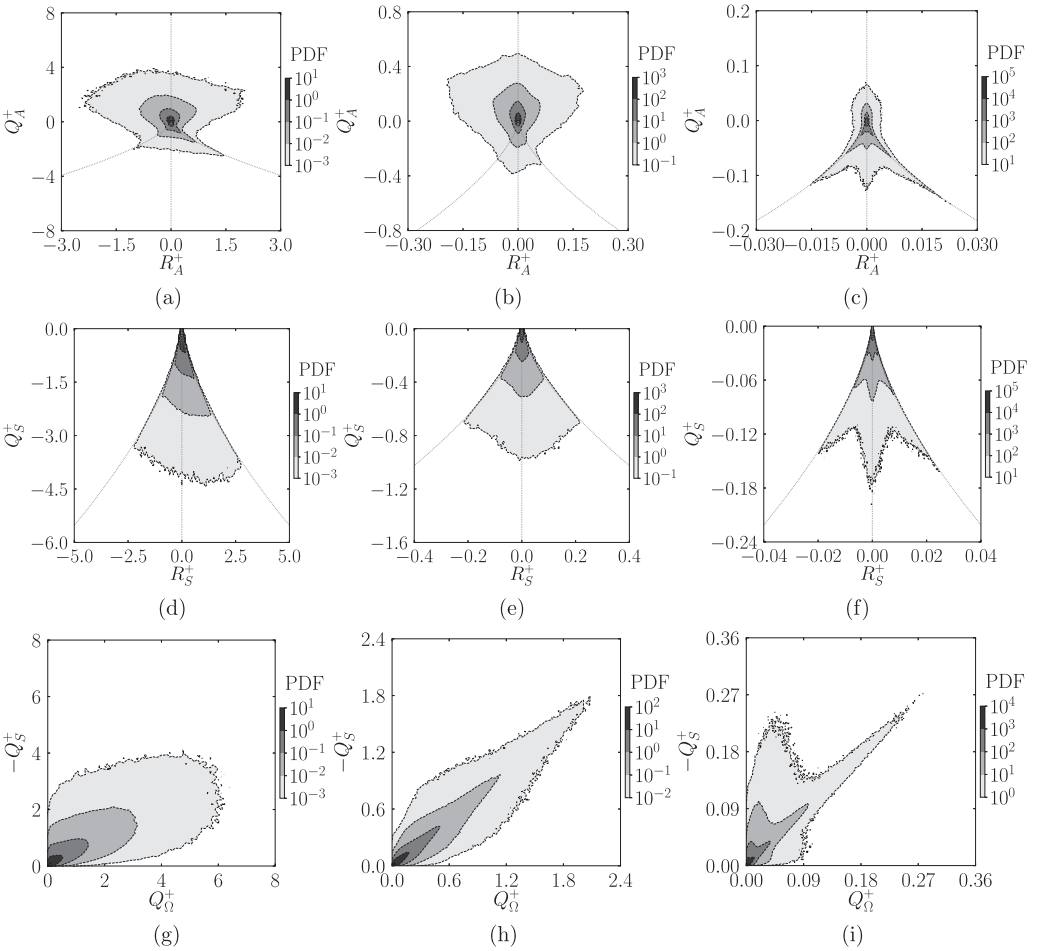

FIG. 10. Joint PDFs of (a–c) Q_A^+ versus R_A^+, (d–f) Q_S^+ versus R_S^+, and (g–h) $-Q_S^+$ versus Q_Ω^+ for cases of increasing viscosity ratio $\gamma =$ (a, d, g) 1, (b, e, h) 10, and (c, f, i) 100 (cases G, C, H) conditioned on $\phi^+ = 1$.

V. CONCLUSIONS

This work reports the joint PDFs of the invariants of the velocity-gradient, rate-of-strain, and rate-of-rotation tensors in decaying isotropic turbulence laden with finite-size droplets ($D_0/\eta = 20$). The joint PDFs were computed in the carrier phase for different distances from the interface using a novel conditional averaging procedure. Four distinct regions of local flow topology with respect to the mean droplet boundary layer thickness δ are identified:

(1) An outer region ($\phi > \delta$) where the flow topologies show a preference for stable focus/stretching ($Q_A > 0$ and $R_A < 0$) and unstable node/saddle/saddle ($Q_A < 0$ and $R_A > 0$) topologies that closely resemble canonical isotropic turbulence.

(2) A transition region ($\phi \approx \delta$) marked by a shift in the skewness of the joint PDF of Q_Ω and $-Q_S$ from a preference for high enstrophy/low dissipation ($Q_\Omega > -Q_S$) to high dissipation/low enstrophy ($-Q_S > Q_\Omega$). The transition is also apparent in the joint PDFs of Q_A versus R_A, which show a marked increase in density along the Vieillefosse tail, the region of (Q_A, R_A)-space where strain production is highest.

(3) An inner region ($\phi < \delta$, $\phi^+ > 1$) denoted by an increased density of $Q_\omega = -Q_S$, which is characteristic of boundary-layer flows with a predominance of vortex sheets.

(4) A viscous region dominated by boundary-layer-like flow topologies leading to clustering at $Q_A = 0$ and $R_A = 0$. The probability of axial and biaxial straining motions becomes equal, as denoted by symmetry about the R_S-axis in the Q_S versus R_S PDF.

The effect of increasing the droplet Weber number was to decrease the mean interfacial shear stress and viscous length scale at the droplet surface. The joint PDFs of Q_S and Q_Ω showed that the probability of vortex sheet topologies near the droplet surface increased with increasing Weber number. Increasing the density and viscosity ratio between the droplet and carrier fluid lead to an increase in interfacial shear stress and showed that in all cases the most dissipative motions near the droplet surface were primarily vortex sheet structures.

Our view is that accurately capturing the velocity gradient near the droplet interface is crucial for the accurate prediction of the dissipation rate of TKE as well as the viscous coupling force between the carrier and droplet phases. Inadequate numerical resolution in DNS or inaccurate SGS models in an LES framework will lead to incorrect turbulent energetics and droplet dynamics. The similarities between the small-scale flow topologies in droplet-laden isotropic turbulence and turbulent wall flows suggest that models in the latter could be applied or adapted to the former. A possible modeling paradigm would resolve the smallest length scales of the bulk flow, use a reduced number of grid points per droplet diameter to capture the droplet interface (e.g., $N_{\mathrm{gp,d}} = 8$ instead of 32), and apply a wall model to accurately predict the shear stress induced by the droplet.

ACKNOWLEDGMENTS

M.S.D. acknowledges support from the Office of Naval Research (ONR), under Grant (or Contract) No. N00014-15-1-2726. L.J. acknowledges support from the Advanced Simulation and Computing (ASC) program of the US Department of Energy's National Nuclear Security Administration via the PSAAP-II Center at Stanford University, Grant No. DE-NA0002373. This work used the Extreme Science and Engineering Discovery Environment (XSEDE), which is supported by the National Science Foundation (NSF), Grant No. ACI-1548562. In particular, the authors acknowledge the Texas Advanced Computing Center (TACC) at The University of Texas at Austin through Allocation No. TG-CTS180029 for providing high-performance computing resources that have contributed to the research results reported within this paper. The authors thank the anonymous reviewers for their valuable comments and suggestions to help improve the quality of the paper.

[1] J. C. Lasheras and E. J. Hopfinger, Liquid jet instability and atomization in a coaxial gas stream, Annu. Rev. Fluid Mech. **32**, 275 (2000).

[2] W. W. Grabowski and L.-P. Wang, Growth of cloud droplets in a turbulent environment, Annu. Rev. Fluid Mech. **45**, 293 (2013).

[3] M. S. Dodd and A Ferrante, On the interaction of Taylor lengthscale size droplets and isotropic turbulence, J. Fluid Mech. **806**, 356 (2016).

[4] J. Hasslberger, M. Klein, and N. Chakraborty, Flow topologies in bubble-induced turbulence: A direct numerical simulation analysis, J. Fluid Mech. **857**, 270 (2018).

[5] D. C. Wilcox, *Turbulence Modeling for CFD* (DCW Industries, La Canada, CA, 1998).

[6] R. H. Kraichnan, Small-scale structure of a scalar field convected by turbulence, Phys. Fluids **11**, 945 (1968).

[7] K. R. Sreenivasan, On local isotropy of passive scalars in turbulent shear flows, Proc. R. Soc. London A **434**, 165 (1991).

[8] K. R. Sreenivasan and R. A. Antonia, The phenomenology of small-scale turbulence, Annu. Rev. Fluid Mech. **29**, 435 (1997).

[9] C. Renner, J. Peinke, R. Friedrich, O. Chanal, and B. Chabaud, Universality of Small Scale Turbulence, Phys. Rev. Lett. **89**, 124502 (2002).
[10] J. Schumacher, J. D. Scheel, D. Krasnov, D. A. Donzis, V. Yakhot, and K. R. Sreenivasan, Small-scale universality of fluid turbulence, Proc. Natl. Acad. Sci. USA **111**, 10961 (2014).
[11] L. Jofre, S. P. Domino, and G. Iaccarino, A framework for characterizing structural uncertainty in large-eddy simulation closures, Flow, Turb. and Combust. **100**, 341 (2018).
[12] L. Jofre, S. P. Domino, and G. Iaccarino, Eigensensitivity analysis of subgrid-scale stresses in large-eddy simulation of a turbulent axisymmetric jet, Int. J. Heat Fluid Fl. **77**, 314 (2019).
[13] F. Lucci, A. Ferrante, and S. Elghobashi, Modulation of isotropic turbulence by particles of Taylor length-scale size, J. Fluid Mech. **650**, 5 (2010).
[14] A. E. Perry and M. S. Chong, A description of eddying motions and flow patterns using critical-point concepts, Annu. Rev. Fluid Mech. **19**, 125 (1987).
[15] M. S. Chong, A. E. Perry, and B. J. Cantwell, A general classification of three-dimensional flow fields, Phys. Fluids A **2**, 765 (1990).
[16] J. Soria, R. Sondergaard, B. J. Cantwell, M. S. Chong, and A. E. Perry, A study of the fine-scale motions of incompressible time-developing mixing layers, Phys. Fluids **6**, 871 (1994).
[17] O. N. Boratav and R. B. Pelz, On the local topology evolution of a high-symmetry flow, Phys. Fluids **7**, 1712 (1995).
[18] J. M. Chacín, B. J. Cantwell, and S. J. Kline, Study of turbulent boundary layer structure using the invariants of the velocity gradient tensor, Exp. Therm. Fluid Sci. **13**, 308 (1996).
[19] H. M. Blackburn, N. N. Mansour, and B. J. Cantwell, Topology of fine-scale motions in turbulent channel flow, J. Fluid Mech. **310**, 269 (1996).
[20] C. B. da Silva and J. C. F. Pereira, Invariants of the velocity-gradient, rate-of-strain, and rate-of-rotation tensors across the turbulent/nonturbulent interface in jets, Phys. Fluids **20**, 055101 (2008).
[21] S. Suman and S. S. Girimaji, Velocity gradient invariants and local flow-field topology in compressible turbulence, J. Turbulence **11**, N2 (2010).
[22] C. Meneveau, Lagrangian dynamics and models of the velocity gradient tensor in turbulent flows, Annu. Rev. Fluid Mech. **43**, 219 (2011).
[23] I. Paul and M. S. Dodd, Fine-scale invariants in turbulence generated by rising bubbles, in *Center for Turbulence Research Annual Research Briefs* (Center for Turbulence Research, Stanford University, Stanford, CA, 2018), pp. 65–77.
[24] P. L. Johnson and C. Meneveau, Predicting viscous-range velocity gradient dynamics in large-eddy simulations of turbulence, J. Fluid Mech. **837**, 80 (2018).
[25] A. Baraldi, M. S. Dodd, and A. Ferrante, A mass-conserving volume-of-fluid method: Volume tracking and droplet surface-tension in incompressible isotropic turbulence, Comput. Fluids **96**, 322 (2014).
[26] M. S. Dodd and A. Ferrante, A fast pressure-correction method for incompressible two-fluid flows, J. Comput. Phys. **273**, 416 (2014).
[27] T. Lewiner, H. Lopes, A. W. Vieira, and G. Tavares, Efficient implementation of Marching Cubes' cases with topological guarantees, J. Graph. Tools **8**, 1 (2003).
[28] A. Ooi, J. Martin, J. Soria, and M. S. Chong, A study of the evolution and characteristics of the invariants of the velocity-gradient tensor in isotropic turbulence, J. Fluid Mech. **381**, 141 (1999).
[29] R. Sondergaard, J. Chen, J. Soria, and B. Cantwell, Local topology of small scale motions in turbulent shear flows, in *Proceedings of the 8th Symposium on Turbulent Shear Flows* (Pennsylvania State University, University Park, PA, 1991), Vol. 1, pp. 16-1-1–16-1-6.
[30] H. Schlichting, *Boundary-Layer Theory* (McGraw-Hill, New York, 1979).